Volume 11 | Number 4 | 28 January 2015 | Pages 637–808

Soft Matter

www.softmatter.org

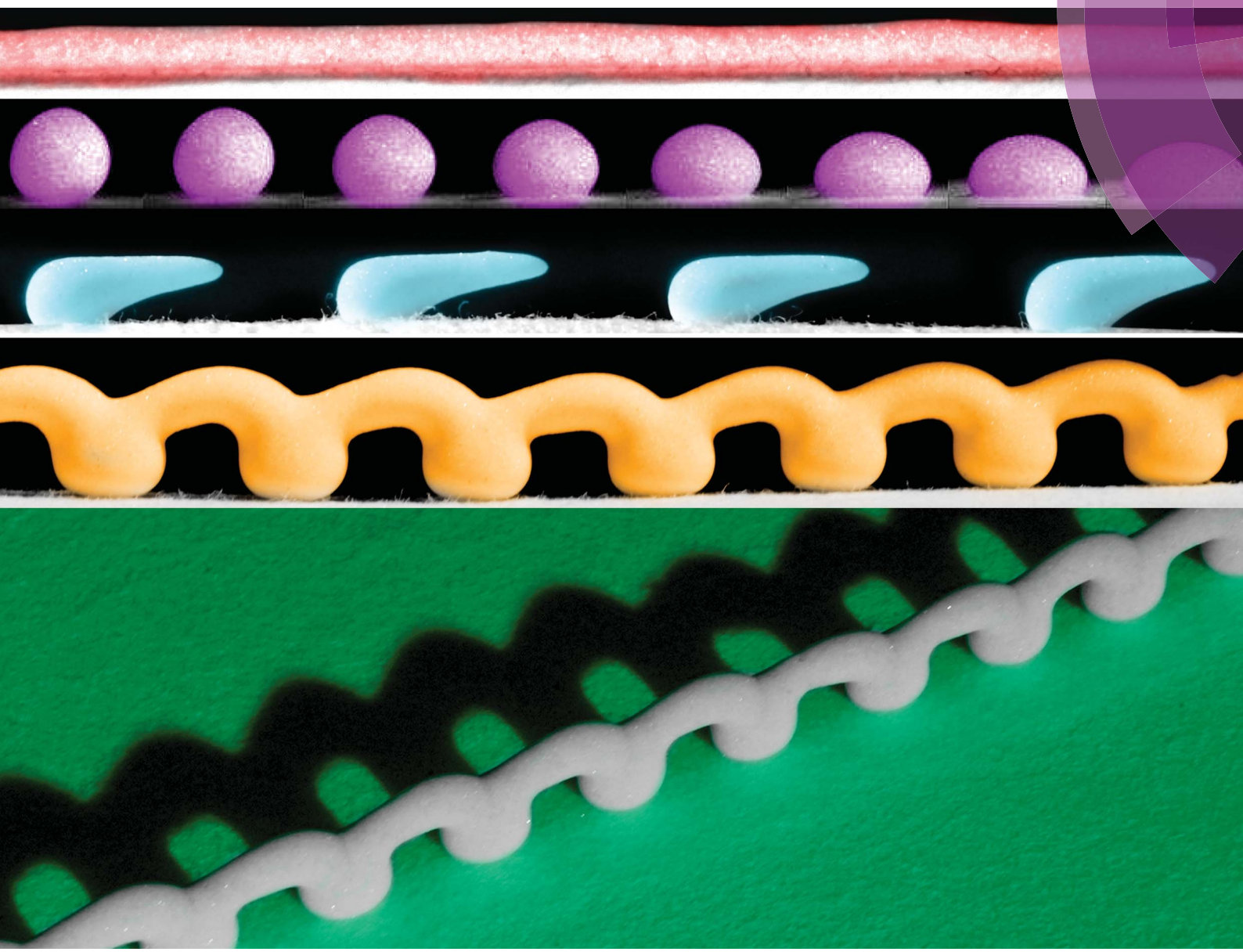

ISSN 1744-683X

ROYAL SOCIETY OF CHEMISTRY

PAPER
Julien Chopin and Arshad Kudrolli
Pearling and arching instabilities of a granular suspension on a super-absorbing surface

Soft Matter

PAPER

View Article Online
View Journal | View Issue

Cite this: *Soft Matter*, 2015, **11**, 659

Pearling and arching instabilities of a granular suspension on a super-absorbing surface†

Julien Chopin* and Arshad Kudrolli

We show that a granular suspension, composed of particles immersed in a liquid, can form pearls, hooks, and arches when deposited from a nozzle onto a translating substrate that acts as a liquid super-absorber. The removal of the liquid induces a rapid pinning of the contact line leading to mechanically stable structures that are held together by capillary adhesion with shapes that depend on the relative solidification rate. Pearls or hooks form depending on whether the suspension snaps off before or after coming into contact with the substrate. A cylindrical thread with a near circular cross-section and various undulatory structures forms if solidification occurs prior to snap-off. In particular, when the jet solidifies before coming into contact with the substrate, it folds periodically, resulting in arches with a span length determined by the deposition flux and the substrate speed. Period doubling and meandering are observed leading to further structures with vertical and horizontal ripples when the deposition flux is increased.

Received 6th October 2014
Accepted 24th November 2014

DOI: 10.1039/c4sm02212b

www.rsc.org/softmatter

1 Introduction

The process by which a liquid drop or jet impacting on a surface undergoes solidification is important in many natural processes and technological applications as in the formation of ice and lava stalagmites, thermal spray coating,[1] inkjet printing,[2] and 3D writing.[3–5] While significant fundamental research has focused on the hydrodynamic instabilities of a homogeneous fluid experiencing dripping,[6] splashing,[7,8] and dewetting,[9] the understanding of the coupling between the flow dynamics and solidification is still in its infancy. In particular, most experiments and simulations are in a regime of slow solidification (that may further include a phase transition or chemical reaction) which only results in a perturbation of the spreading dynamics on a surface.[10,11]

Recently, we demonstrated that a granular suspension dripped onto a substrate leads to the growth of intricate tower structures that are held together by capillary cohesion.[12] The necessary condition was that the substrate should act as a super-absorber for the liquid in the suspension. Here, we show that such a rapid solidification coupled with instabilities (Rayleigh–Plateau or jet breakup, stick–slip contact line dynamics, *etc.*) can lead to novel compact and undulatory structures on a super-absorbing surface which translates horizontally. The translation rate gives rise to a further timescale which is important for the formation of the observed structures. In contrast to intricate weaving patterns observed with a Newtonian fluid,[13–15] we show that the observed structures which include pearls, hooks, and arches are not only three-dimensional and mechanically stable, but also have a different physical origin because of rapid solidification. In addition to finding novel coupling between solidification and hydrodynamical instabilities, our work can be viewed as providing an alternative strategy to wet granulation and moulding to deliver and shape amorphous powders. A significant advantage is that the powder can be suspended and transported in a liquid medium at ambient temperature, which can be drawn away, as the desired form is attained.

2 Experimental

A schematic of the experimental system along with the control parameters is shown in Fig. 1A. A nozzle with diameter d attached to a pump syringe is located at height H vertically above a substrate which is mounted on a horizontal translating stage driven by a stepper motor. Nozzles with an inner diameter of $d = 1.2$, 1.6, and 2.0 mm are used. The substrate speed V_s is varied between 1 and 20 cm s^{-1}. Unless otherwise stated, a blotting paper is used as the liquid absorbing substrate with the absorption strength characterized by a liquid absorption coefficient in the medium $D = 4 \times 10^{-6}$ m^2 s^{-1} (Fig. S1) (see ESI†). The substrate needs to have sufficiently high absorption strength for fast drainage and solidification and is thus called the super-absorber.

The granular suspension used consists of glass beads with a radius of $a = 17 \pm 10$ μm immersed in water with a viscosity of $\mu = 0.9$ mPa s and a surface tension of $\gamma \approx 70$ mN m^{-2}. A

Department of Physics, Clark University, Worcester, MA 01610, USA. E-mail: jchopin@clarku.edu; akudrolli@clarku.edu

† Electronic supplementary information (ESI) available. See DOI: 10.1039/c4sm02212b

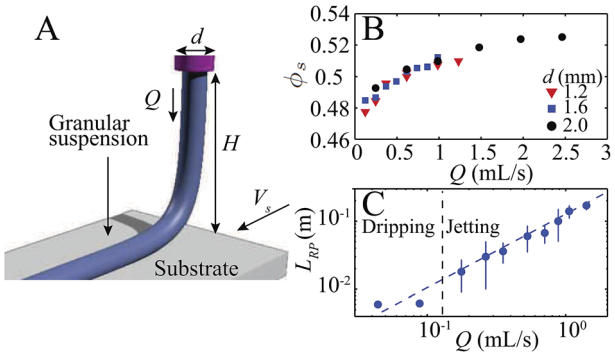

Fig. 1 (A) A schematic of a granular suspension emerging from a nozzle with a flux Q and falling as a uniform thread onto a substrate translating with a speed V_s. (B) The solid volume fraction ϕ_s of the suspension emerging from the nozzle is observed to increase with Q and is essentially independent of the nozzle diameter d. (C) The jet length L_{RP} before it breaks up into droplets due to a Rayleigh–Plateau-like instability is observed to increase linearly with Q in the jetting regime. The transition from dripping to jetting occurs at $Q \sim 0.15$ mL s^{-1}.

suspension is prepared by first pouring 30 mL of liquid into a 60 mL syringe and then filling it with glass beads which sediment to the bottom. A stepper motor is used to control Q over the range 0.01–2.0 mL s^{-1}. The volume fraction of the glass beads in the suspension ϕ_s which emerges from the nozzle is seen to increase slowly with Q as shown in Fig. 1B (see ESI† for methods). This trend shows that the liquid entrains more grains with Q as it moves through the sedimented bed inside the syringe. We also find that the granular suspension transitions from emerging as a drop to a jet near the nozzle at $Q \sim 0.15$ mL s^{-1}. However, because a uniform jet will eventually break-up into drops because of a Rayleigh–Plateau-like instability,[16] we measure the distance through which the suspension falls L_{RP} during that time in Fig. 1C. Thus, by using an appropriate H, one can choose whether the suspension impacts the substrate as a drop or as a continuous jet.

Examples of the structures obtained depending on the various instabilities and their sequences relative to solidification are shown in Fig. 2 and Movies S1–S4.† In the jetting regime and for $H < L_{RP}$, we find a continuous cylindrical thread as shown in Fig. 2A and Movie S2† at relatively high V_s and Q. This uniform thread is measured to have a large contact angle with the substrate ($\theta_c \approx 140$ degree) and may be considered as the base state of the system. By choosing Q in the dripping regime, we find that a spherical or oblate pearl forms depending on H (see Fig. 2B and Movie S3†). Hooks are obtained when the snap off and solidification occur well after the suspension comes into contact with the substrate (see Fig. 1C and Movie S4†). The effect of solidification is even more dramatic at lower substrate speed when we observe the spontaneous emergence of arches with periodic contact with the substrate as the contact line performs stick–slip motion (see Fig. 2D and Movie S1†).

These structures are fully self-supporting as seen in Fig. 2E. It may be noted that they are held together by the cohesive forces which arise in the residual liquid which remain between the grains in the suspension. In the laboratory, we have found that the reported structures survive for days if not months as the residual liquid evaporates and develops weak Si–O–Si bonds.[17] The addition of binders into the suspending liquid phase, for example, can enhance the binding strength between grains after the residual liquid evaporates allowing structures to be assembled from amorphous solids. However, this is not a focus of the study here, and we do not discuss it further.

In order to understand the relative importance of the main control parameters in our experiments, we introduce a dimensionless substrate speed Su $= V_s/V_{fl}$, which corresponds to the ratio of the substrate speed V_s and the flow speed of the suspension out of the nozzle V_{fl} given by $4Q/(\pi d^2)$ in the jetting regime and by the impact velocity V_i in the dripping regime. Further, we introduce a second dimensionless number, the dripping number Dr $= H/L_{RP}$, where Dr > 1 corresponds to the dripping regime, and Dr < 1 corresponds to the jetting regime. With this definition, it appears as if Dr is independent of V_s because L_{RP} is measured here without a substrate. However, this is not true when the suspension falls on to a substrate in the regime where Dr is small and V_s is large, because the contact with the substrate due to its relative motion results in dragging and stretching of the liquid jet before it freezes or snaps off. As we will see later, this additional dynamics plays an important role in the formation of the structures observed in this regime. Finally, we introduce a third dimensionless number Ab $= \tau_S/\tau_D$ which is the ratio of the spreading timescale τ_S and drainage timescale τ_D. When Ab $= 0$, the suspension spreads like an effective viscous fluid without solidification. When Ab $\gg 0$, the suspension solidifies with little spreading.

We now discuss how the three non-dimensional parameters Su, Dr, and Ab allow us to organize a phase diagram of the various observed structures. To aid visualization, we plot the projection of the 3D phase diagram in the Ab–Dr plane (Fig. 2F) and along the line Su (Fig. 2G). In the Ab–Dr plane, four regions are identified. Cylindrical threads are obtained for Ab < 1, *i.e.* a relatively slow solidification rate. Pearls, hooks and arches are obtained for Ab > 1. Interestingly, discontinuous structures (hooks) can be obtained when Dr < 1 but for large Ab and Su. Indeed, the jet is dragged by the substrate in the hook regime (due to small H or Dr < 1) by stretching it and ultimately leading the jet to snap off, when Su $\gg 1$.

3 Pearling

To understand the process by which these structures form, we next examine their physical features and the conditions under which they occur, in more detail. In particular, we provide the scalings for the three dimensionless numbers allowing us to add experimental data on the phase diagram. Fig. 3A shows a plot of the height to width aspect ratio A_r of the pearls to capture the degree of sphericity along with the contact angle with the substrate θ_c as a function of impact speed V_i. While $A_r \sim 1$ for low V_i and then decreases, θ_c remains obtuse and roughly constant over the larger range of V_i. These shapes are thus reminiscent of liquid drops present on a hydrophobic substrate, which may appear surprising given the hydrophilic nature of

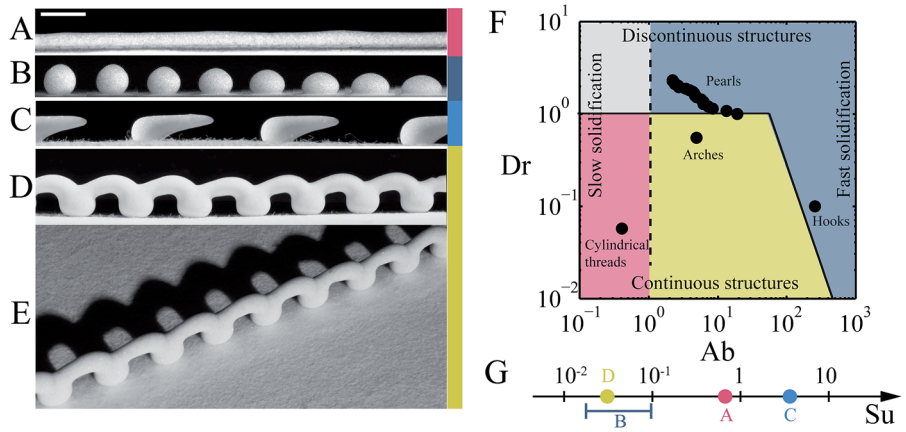

Fig. 2 Examples of solidified structures obtained due to pearling and arching instabilities. (A) A cylindrical thread corresponding to the base state of the system is observed when arching and pearling instabilities do not have time to develop before solidification ($d = 2.0$ mm, $Q = 0.35$ mL s^{-1}, $V_s = 9.7$ cm s^{-1}). (B) Spherical to oblate axisymmetric pearls form in the dripping regime when H is varied linearly from 6 mm to 14 mm from left to right ($d = 1.2$ mm, $Q = 0.044$ mL s^{-1}). (C) Hook shapes are obtained when the snap off occurs after the drop comes into contact with the super-absorbing substrate and solidification reaches the bridge connecting the drop and the nozzle ($d = 2.0$ mm, $Q = 0.18$ mL s^{-1}, $V_s = 2.4$ cm s^{-1}, $H =$ 2.5 mm). (D) Periodic arches are observed when the solidification rises up the thread in the jetting regime which folds because of gravity and solidifies ($d = 2.0$ mm, $Q = 0.18$ mL s^{-1}, $V_s = 1.2$ cm s^{-1}, $H = 10$ mm). (E) The same arches viewed in perspective illustrate their 3D nature. Scale bar is 4 mm. (F) Phase diagram in the Ab–Dr plane showing four different regimes depending on the relative solidification rate (Ab > 1 and Ab < 1) and flow regime (jetting and dripping). Ab and Dr are the absorption and dripping numbers respectively (see text for their definitions). Black disks correspond to the experimental data shown in A to E. (G) The same data are organized along the Su-axis highlighting, in particular, that hooks form at high substrate speed (Su $\gg$ 1). Su is the dimensionless substrate speed (see text for its definition).

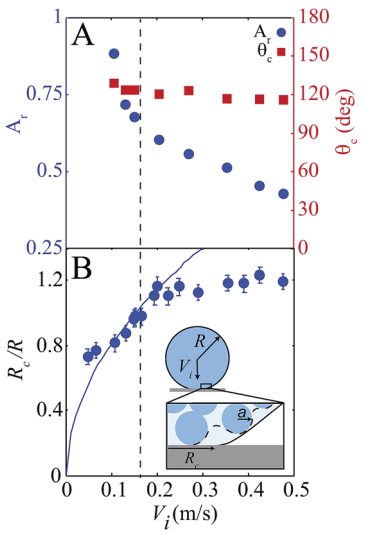

Fig. 3 Illustration of the effect of solidification on the equilibrium shape of a pearl. (A) The aspect ratio A_r of a pearl is observed to decrease with V_i while the contact angle with the substrate θ_c is roughly constant and is surprisingly high for a water-based suspension spreading on a hydrophilic substrate. These shapes illustrate the strong effect of solidification. The experimental parameters are the same as in Fig. 2B. (B) The normalized contact radius R_c/R as a function of V_i is fitted using eqn (1) below $V_i = 0.16$ cm s^{-1} (blue line) with $\tau_D = 7.2$ ms. Inset: schematics of a drop upon impact with a close-up of the contact line.

the super-absorbing surface. However, we can understand these shapes by the fact that the solidification rapidly pins the contact line (CL) when a small volume of liquid is drained near the CL, leading to a rough air/liquid/grain interface as illustrated in the inset of Fig. 3B. Such an interface causes a yield stress to develop because of the capillary cohesion and friction between particles at the surface.[12]

We plot the measured radius of the contact area R_c scaled by the radius R of the drop prior to contact as a function of V_i in Fig. 3B. R_c/R appears to have a finite value at low V_i and grows non-linearly before appearing to plateau at higher V_i. This trend can be understood from the fact that a certain time is required for the excess liquid to drain, which will yield a very small contact area when the impact speed is low. However, as V_i increases the contact area can be expected to grow because greater kinetic energy is available to overcome viscous dissipation of the drop before it solidifies. We therefore consider the characteristic timescale τ_D for the drainage of a thin liquid layer of thickness ξ after the suspension first comes into contact with the substrate. Over this time, the drop spreads on the substrate and forms a contact area with a radius given by:

$$R_c/R \sim \sqrt{\tau_D V_i/R}. \quad (1)$$

This estimate is obtained using a simple geometric argument which assumes a spherical drop and is thus valid for small deformations ($R_c/R \ll 1$), *i.e.* for times shorter than the impact duration $\tau_i \sim R/V_i$. Forcing a fit of the experimental data for $V_i <$ 0.16 m s^{-1} (corresponding to $\tau_i >$ 7.5 ms) with τ_D as the adjustable parameter, we find $\tau_D = 7.2$ ms. Further, using an imbibition mechanism, τ_D, D, and ξ are found to be linked by the dimensional relationship:

$$\tau_D \sim \xi^2/D \quad (2)$$

We are unable to measure ξ directly, but we can estimate it from the solid volume fraction both before and after impact, $\phi_s \approx 50\%$ and $\phi_s^* \approx 63\%$, respectively. Hence, $\xi \approx (R/3)(\phi_s^* - \phi_s)/\phi_s \sim 100$ μm. Thus, our model gives $\tau_D \sim 2.5$ ms which is of the same order of magnitude, as previously estimated. Using this model, we can give a scaling for the various dimensionless numbers. In the pearling regime, we have Ab $\sim RD/(V_i\xi^2)$, assuming that $\tau_s \sim \tau_i$ and Su $\sim V_s/V_i$ where we used the fact that $V_{fl} \sim V_i$. Using experimental data from Fig. 2, we obtain Ab in the range 0.5–20 and Su in the range 0.02–0.1. Overall, we find that at low impact speed, drainage is faster than the impact (Ab > 1), which results in pearls that are solidified in a configuration, far from equilibrium.

4 Hook formation

We next discuss the hooks which form when a snap off occurs after the drop comes into contact with the substrate as shown in the sequence of images in Fig. 4A and Movie S4.† This occurs for small Dr (<1) and large Su (in the range 5–50). The solid phase can be noted to first grow off the substrate and the liquid thread is stretched. After snap off, the tips recede somewhat on the side attached to the substrate, and fully on the side attached to the nozzle. Fig. 4B shows the minimal waist of the liquid thread w. For $t > t_0$ set by the substrate speed, we use a function typically used to describe the waist of a liquid bridge undergoing pinch off:[18]

$$w(t) = w(t_0)\exp(-V_s(t - t_0)/2\zeta), \quad (3)$$

with ζ as a fitting parameter. An exponential fit is observed for several V_s with $\zeta \approx 2.7$ mm which is the typical length of the liquid thread. Due to its kinematic origin, the decrease of the waist is essentially independent of the fluid rheology. Then, for small waist ($w \sim 0.6$ mm) capillary effects become dominant resulting in an accelerated thinning of the thread until snap off occurs at time t_b. In Fig. 4C, we plot log–log $w/w(t_0)$ as a function of τ/t_0 varying the substrate speed, where $\tau = t_b - t$ is the time from break-up. The minimal waist is found to scale as $(\tau/t_0)^\alpha$ with an exponent α that depends on the substrate speed. At high speed ($V_s \geq 9.8$ cm s^{-1}), we measure $\alpha = 0.53 \pm 0.05$ which is clearly different from Newtonian fluids ($\alpha = 1$)[19] and smaller than observed previously with dense suspensions ($\alpha = 2/3$).[20] A still smaller exponent ($\alpha = 0.35 \pm 0.05$) is measured at a lower speed ($V_s = 4.8$ cm s^{-1}) which may be due to the fact that the suspension is on the verge of solidification at snap off.

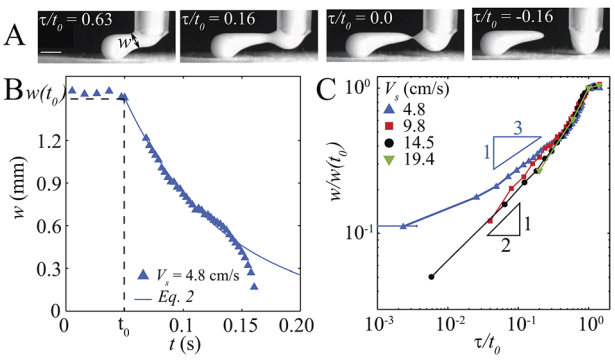

Fig. 4 Hook formation and anomalous pinch off dynamics of a stretched solidifying liquid bridge. (A) Sequence of hook formation (thick blotter, $d = 2.0$ mm, $Q = 0.088$ mL s^{-1}, $V_s = 4.8$ cm s^{-1}, $H = 2.5$ mm). Scale bar is 2 mm. (B) Temporal evolution of the liquid bridge waist w where an exponential thinning is observed. From a fit of the data (solid line), we measure $\zeta \approx 2.7$ mm. (C) $w/w(t_0)$ as a function of the normalized time to breakup τ/t_0 for a fixed flux $Q = 0.88$ mL s^{-1} and varying V_s. For high substrate speed, the diameter follows the scaling $w \sim t^\alpha$ with ($\alpha = 0.53 \pm 0.05$) while a qualitatively different dynamics is observed at a lower substrate speed ($V_s = 4.8$ cm s^{-1}) with ($\alpha = 0.35 \pm 0.05$).

5 Arching

When V_s is lowered further, pinch off does not occur and a continuous thread falls on and off the substrate resulting in arches (Fig. 2G and Movie S1†). This occurs because the solidification rate of the thread up off the substrate slows down with height, and the fluid region of the thread falls back on the substrate because of gravity, which then quickly solidifies upon contact in the shape of an arch. This process then repeats itself giving rise to various undulatory structures besides arches. In Fig. 5A–C, we show the structures obtained by increasing the suspension flux while keeping V_s constant. At low flux, slender arches are obtained. When the flux is increased, due to volume conservation, the arches are thicker and thus the undulations appear with smaller amplitudes and resemble ripples. The key difference is that the solidification front rises up the jet in the case of arches, whereas solidification occurs after the jet comes into contact with the substrate in the case of ripples. This fact can be seen from the bright spot in the images (Fig. 5A–C), which indicates the presence of a thin superficial liquid layer reflecting light.

Further, as Q is increased, period doubling can lead to superposition of ripples and arches (see Movie S5†), and at still larger Q, the structure is decorated by ripples that oscillate sideways (see Movie S6†). Although this meandering instability is reminiscent of the coiling of a purely viscous jet on a translating substrate,[13] the mechanism is different here because it does not rely on a viscous buckling instability, but rather on the pinning of the contact line and solidification.

The undulating structures can be characterized quantitatively by measuring the span and base lengths, l_s and l_b, respectively. We find that l_s reaches a maximum with respect to Q (Fig. 5D) and V_s (Fig. 5E) while l_b is approximately Q-independent and increases continuously with V_s. Therefore a specific combination of the flow rate and substrate speed results in an optimal span length. This optimal length can be understood from the tower growth model[12] and the CL pinning introduced in the discussion on the drop impact analysis previously. Arches can be thought to develop as leaning towers growing with an angle α with respect to the substrate (see Fig. 5A) reaching their maximum height h_X before falling. Thus, $h_X \sim \Phi D/v_G$, where $v_G = (\phi/\phi^*)Q/s$ is the growth velocity, s the arch cross-section, $\Phi = \phi_s/(\phi_s^* - \phi_s)$, and ϕ_s^* the solid volume fraction after solidification. v_G is of the order of 20 cm s^{-1} and

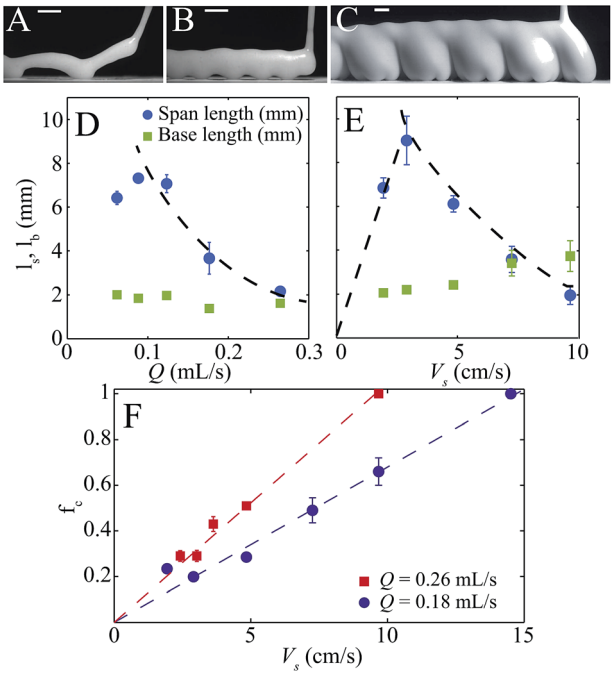

Fig. 5 Images of undulating structures obtained by increasing the flux Q including (A) arches (thin blotter, $Q = 0.12$ mL s^{-1}, $V_s = 2.4$ cm s^{-1}, $d = 1.19$ mm), (B) ripples (thin blotter, $Q = 0.26$ mL s^{-1}, $V_s = 2.4$ cm s^{-1}, $d = 1.19$ mm) and (C) meandering bumps (thick blotter, $Q = 1.76$ mL s^{-1}, $V_s = 1.2$ cm s^{-1}, $d = 2.0$ mm). Arches are characterized by the span distance and a base length. Scale bars are 4 mm. (D) Evolution of the span (green squares) and base length (blue disks) at a flow rate of $V_s = 2.4$ cm s^{-1}. A sharp decrease of the spacing is observed for $Q \sim 0.15$ mL s^{-1} separating the arch mode with the ripple mode. (E) Base and span lengths as a function of the substrate speed V_s at $Q = 0.18$ mL s^{-1}. (F) Evolution of the fractional contact length f_c with V_s for two flow rates $Q = 0.18$ mL s^{-1} and $Q = 0.26$ mL s^{-1} showing a linear increase.

always smaller than V_s. The arch span length is then defined as the projected height on the substrate $l_s \sim h_X \cos \alpha$ where $\cos \alpha \approx V_s/v_g$ (for $V_s \ll v_G$) yielding $l_s \sim \Phi D V_s/v_G^2$. This law captures qualitatively the decrease with Q and the increase with V_s at low substrate speed. The maximum observed with Q may be attributed to the influence of the nozzle which constrains the tower height. This constraint is observed at small Q, because H has to be decreased accordingly to avoid dripping.

Next, to understand the decrease of l_s with V_s at higher substrate speed, we measure the fractional contact length defined as $f_c = l_b/(l_s + l_b)$ $(0 < f_c \leq 1)$ for different flow rates by varying the substrate speed (Fig. 5F). f_c is found to increase linearly with the substrate speed until the arch instability is completely suppressed ($f_c = 1$) which occurs at $V_s = 14.6$ cm s^{-1} for $Q = 0.18$ mL s^{-1} and $V_s = 9.5$ cm s^{-1} at $Q = 0.26$ mL s^{-1}. The shape obtained is thus a cylindrical thread which is in constant contact with the substrate along its length. In this regime, the CL speed is simply V_s and the characteristic time for spreading is then $\tau_S \sim \xi/V_s$ which is the time to renew a volume of typical size ξ near the CL. Solidification is not fast enough to pin the contact line when $\tau_S \sim \tau_D$, yielding a crossover speed $V_s^X \sim D/\xi \sim 2$ cm s^{-1} which corresponds to the maximum observed in Fig. 5D. When $V_s > V_s^X$, the thread falling back on the substrate experiences an extended spreading before being pinned resulting in larger l_b and smaller l_s due to a comparatively slow solidification rate.

We can now give the scaling for Ab in the cylindrical and arch regime. Using eqn (2) and $\tau_S \sim \xi/V_s$, we obtain Ab $\sim D/(V_s\xi)$ which is ~0.4 in the cylindrical regime and ~4 in the arch regime. However, the formation of arches involves periodic impacts of the thread on the substrate, therefore, Ab is best estimated using the scaling of the pearl regime, yielding Ab in the range 5–10^2 depending on the impact speed which can vary from 1 to 30 cm s^{-1}.

6 Conclusions and perspectives

In conclusion, we have shown that a new class of structures arise in rapidly solidifying flows driven by a rapid removal of a liquid from a dense suspension as it comes into contact with a liquid super-absorber along with other dynamical instabilities. These structures go well beyond the vertical slender tower structures, we have demonstrated previously,[12] which arise when a granular suspension is dripped onto a stationary substrate. We find that a variety of shapes including spherical and oblate pearls, arches, and hooks can spontaneously form depending on the liquid absorption rate, the degree of spreading, flux, and substrate speed.

Accordingly, we introduce three dimensionless numbers Su, Dr, and Ab, which capture the ratio of the substrate and flux velocity, the drop height relative to the length of the emerging jet before it breaks up, and spreading and absorption time scales, respectively to organize a phase diagram covering the various regimes investigated. Using these three-dimensionless numbers, one can understand the overall features observed in the phase diagram and the conditions under which they occur. In particular, when Ab > 1, pearls occur for Dr > 1 and hooks for Dr < 1 and large Su. At moderate Su and Dr < 1, arches are obtained. For smaller Ab (<1), the observed structures are the cylindrical threads.

Further, unlike a viscous Newtonian fluid which gives rise to various meandering patterns in a thin horizontal layer which is in contact with the substrate, and thus essentially two-dimensional,[13–15] the structures obtained are three-dimensional. Because of the paramount importance of liquid absorption and solidification, the origin of the structures is also quite different from that for a viscous thread interacting with a substrate where gravity and viscous forces set the length and time scales relative to translation. Thus, the spreading dynamics where the flow over the substrate is coupled with a solidifying process yields a rich set of patterns which underlies a complex non-linear dynamical system. In this context, it would be interesting to consider how one can move from one limit to the other by changing the viscosity of the suspending fluid which will progressively reduce the drainage rate but introduce viscous force. However, this is beyond the scope of this investigation.

Finally, our study offers not only an opportunity to develop granular suspension models which undergo rapid jamming, but also applications as mentioned in the Introduction. Specifically, current 3D printer matrices rely on using a

temporary filling which needs to be dissolved away to create an arch or dome-like structure. This is not only cumbersome but also not feasible when a hole is desired which cannot be reached after assembly of the structure. The demonstration of the formation of arches, besides other rich varieties of structures, suggests the potential of granular suspensions and our technique towards such applications.

Acknowledgements

We thank Pascal Jundt and Suyesh Thapa for their help with experiments.

References

1 P. Fauchais, A. Vardelle, M. Vardelle and M. Fukumoto, *J. Therm. Spray Technol.*, 2004, **13**, 337–360.
2 P. Calvert, *Chem. Mater.*, 2001, **13**, 3299.
3 F. Gao and A. A. Sonin, *Proc. R. Soc. London, Ser. A*, 1994, **444**, 533–554.
4 J. A. Lewis, *Adv. Funct. Mater.*, 2006, **16**, 2193–2204.
5 Y. Gao, H. Li and J. Liu, *PLoS One*, 2012, **7**, e45485.
6 J. Eggers and E. Villermaux, *Rep. Prog. Phys.*, 2008, **71**, 036601.
7 A. L. Yarin, *Annu. Rev. Fluid Mech.*, 2006, **38**, 159.
8 L. A. Lubbers, Q. Xu, S. Wilken, W. W. Zhang and H. M. Jaeger, *Phys. Rev. Lett.*, 2014, **113**, 044502.
9 R. Craster and O. Matar, *Rev. Mod. Phys.*, 2009, **81**, 1131.
10 M. Pasandideh-Fard, S. Chandra and J. Mostaghimi, *Int. J. Heat Mass Transfer*, 2002, **45**, 2229–2242.
11 Q. Xu, E. Brown and H. M. Jaeger, *Phys. Rev. E: Stat., Nonlinear, Soft Matter Phys.*, 2013, **87**, 043012.
12 J. Chopin and A. Kudrolli, *Phys. Rev. Lett.*, 2011, **107**, 208304.
13 S. Chiu-Webster and J. R. Lister, *J. Fluid Mech.*, 2006, **569**, 89–112.
14 S. W. Morris, J. H. Dawes, N. M. Ribe and J. R. Lister, *Phys. Rev. E: Stat., Nonlinear, Soft Matter Phys.*, 2008, **77**, 066218.
15 P. Brun, N. Ribe and B. Audoly, *Phys. Fluids*, 2012, **24**, 043102.
16 C. Bonnoit, T. Darnige, E. Clément and A. Lindner, *J. Rheol.*, 2010, **54**, 65.
17 N. Olivi-Tran, N. Fraysse, P. Girard, M. Ramonda and D. Chatain, *Eur. Phys. J. B*, 2002, **25**, 217–222.
18 G. H. McKinley and T. Sridhar, *Annu. Rev. Fluid Mech.*, 2002, **34**, 375–415.
19 J. Eggers, *Rev. Mod. Phys.*, 1997, **69**, 865.
20 M. Miskin and H. Jaeger, *Proc. Natl. Acad. Sci. U. S. A.*, 2012, **109**, 4389.